



BCC-HCP-FCC Multiple Transformations and ε Loop in the Fe-Cr-Co-Mn System

Toshihiro Omori¹ · Keisuke Ando¹ · Ikuo Ohnuma² · Ryosuke Kainuma¹ · Kiyohito Ishida¹

Submitted: 9 April 2021 / in revised form: 20 May 2021 / Accepted: 24 May 2021 / Published online: 28 June 2021
© ASM International 2021

Abstract Phase transformations and phase stability in the Fe-Cr-Co-20Mn (at.%) alloy system were investigated using optical microscopy, transmission electron microscopy, x-ray diffraction, and vibrating sample magnetometry. Thermal-induced martensitic transformation from the BCC α parent phase to the HCP ε martensite phase was observed in the samples with near 36Fe-24Cr-20Co-20Mn compositions. Bainitic transformation from the α phase occurred with aging. Although the α parent phase coexisted with the ε martensite phase in the as-quenched specimen and transformation did not proceed with sub-zero treatment, the ε martensite was completely induced by cold rolling. Furthermore, the FCC γ phase was obtained by heavy deformation. These results indicate that multiple martensitic transformations from α to ε and ε to γ occurred. The $\gamma \rightarrow \varepsilon$ martensitic transformation was also observed for 48Fe-16Cr-16Co-20Mn. The phase stabilities of the α , ε , and γ phases were similar. The calculated T_0 lines successfully predicted the $\alpha \rightarrow \varepsilon$ martensitic transformation when the ε phase was more stable in the database. Thermodynamic analysis revealed that magnetic ordering in the

α phase affected the phase stability, resulting in the novel ε loop in addition to the conventional γ loop.

Keywords CALPHAD · experimental study · phase transformation · thermodynamic stability

1 Introduction

High entropy alloys (HEAs) [1, 2] have received significant attention because of their potential good mechanical properties from cryogenic to high temperatures [3–12] and unique functional properties, including thermal and magnetic properties. [4, 5, 13] The original concept of HEAs is to form a solid solution because of the large configurational entropy in equiatomic or near-equiatomic solid-solution alloys comprising five or more elements. [1, 2] Currently, research on HEAs has expanded to non-equiatomic multi-component alloys, [3, 5, 14, 15] in which alloys comprising three or four elements are termed medium-entropy alloys, [16] and alloys containing secondary phases which can play a role in strengthening. [17–20] Phase stability is a key issue in HEAs. A thermodynamic database using the CALculation of PHase Diagrams (CALPHAD) method has been developed for the alloy design of HEAs. [21–24]

The equiatomic quinary 20Fe-20Cr-20Mn-20Ni-20Co (at%) alloy, known as the Cantor alloy, [2] has a single FCC solid solution and is one of the most popular HEA systems. The Fe-Cr-Co system is a subsystem of Fe-Cr-Mn-Ni-Co. In the Fe-Cr system, Cr stabilizes the α (BCC) phase, and in the Fe-Co system, the γ (FCC) solid solution phase exists from Fe to Co at high temperatures, while α is stable at low temperatures. [25] Magnetic ordering greatly affects the phase stability in Fe and Fe alloys [26] and the α phase is

This article is part of a special topical focus in the Journal of Phase Equilibria and Diffusion on the Thermodynamics and Kinetics of High-Entropy Alloys. This issue was organized by Dr. Michael Gao, National Energy Technology Laboratory; Dr. Ursula Kattner, NIST; Prof. Raymundo Arroyave, Texas A&M University; and the late Dr. John Morral, The Ohio State University.

✉ Toshihiro Omori
omori@material.tohoku.ac.jp

¹ Department of Materials Science, Graduate School of Engineering, Tohoku University, Sendai 980-8579, Japan

² Research Center for Structural Materials, National Institute for Materials Science (NIMS), Tsukuba 305-0047, Japan

stable at low ($T < A_3$) and high ($T > A_4$) temperatures. Therefore, the γ loop is formed when an α -stabilizing element is added to Fe, including in the Fe-Cr system. The γ phase of Fe-Cr expands upon the addition of Co. The FCC solid solution phase is stable in half of the isothermal section of the Fe-Co-rich side at high temperatures, for example at 1300 °C in the Fe-Cr-Co system. Conversely, the BCC solid solution occupies half of the Fe-Cr-rich side. [27, 28] A two-phase region (FCC + BCC) exists between them.

A number of phase transformations occur in the Fe-Cr-Co system. Fe-Cr-Co alloys are permanent magnets with good workability. Magnetic hardening is achieved by the fine microstructure due to the phase separation to FeCo (B2) and Cr (A2). [29–32] Another example is the Co-Fe-Cr Invar alloy [33] where the coefficient of thermal expansion is low at the composition of 54Co–37Fe–9Cr (mass%). Our preliminary study showed that α and ε phases coexist in the γ phase matrix. Although the phase stability of the ε phase has not been well determined compared to those of the α and γ phases in the Fe-Cr-Co system, Co-Cr alloys have a high M_s temperature of the $\gamma \rightarrow \varepsilon$ martensitic transformation. [34] ε is not a stable phase at ambient pressure in Fe, but the $\gamma \rightarrow \varepsilon$ martensitic transformation occurs in the Fe-Mn system. The phase stability of the ε phase in a mixture of Co-Cr and Fe-Mn is of interest from the viewpoint of thermodynamics. In particular, reports on the phase transformation between α and ε phases at atmospheric pressure have been very limited in transition metals, except for Ti, Zr, and Hf-based alloys.

From the information on the phase equilibria and phase transformation in the binary and ternary systems, phase transformations among the α , ε , and γ phases are expected to occur in the Fe-Cr-Co-Mn system. In this study, the phase transformation of the α phase in the Fe-Cr-Co-Mn system was investigated.

2 Experimental and Analytical Procedures

The alloy compositions (at.%) of the Fe-Cr-Co-Mn quaternary alloys are shown in Fig. 1 (20 at.% Mn, except for one 10 at.% Mn alloy). In particular, detailed results will be shown for 36Fe–24Cr–20Co–20Mn (Alloy A), 35.6Fe–24Cr–20.4Co–20Mn (Alloy B), and 35.2Fe–24.8Cr–20Co–20Mn (Alloy C). Ingots with an approximate diameter of 12 mm and a length of 30 mm were produced by induction melting under an Ar atmosphere. They were hot rolled at 1300 °C to a thickness of 2 mm. Small pieces of specimens were sealed in quartz tubes under vacuum and annealed at 1300 °C for 30 min, followed by quenching in water; the annealing temperature and period were respectively 1300 °C and 24 h to determine the phase equilibria.

The microstructure was observed at room temperature by optical microscopy after etching using hydrochloric acid

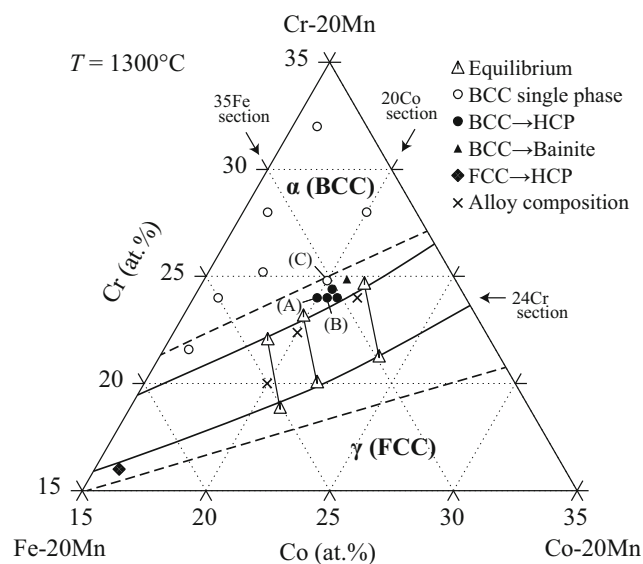


Fig. 1 Isothermal section of the Fe-Cr-Co-20Mn system at 1300 °C. Equilibrium compositions and investigated alloys are indicated. The solid and dashed lines are phase boundaries based on the results of the phase equilibria and calculation using the TCHEA2 database, respectively. Vertical sections of 20Co, 24Cr, and 35Fe are depicted in Figs. 12 and 14

with a few drops of hydrogen peroxide solution. Transmission electron microscopy (TEM) was also performed. The TEM specimens were prepared by mechanical grinding and twin-jet electro-polishing using a solution of 20% perchloric acid and 80% ethanol. The equilibrium compositions were determined using electron probe microanalysis (EPMA). Phase identification was performed using x-ray diffraction (XRD).

Some of the specimens were cold rolled to induce martensite formation. To heavily deform the specimens, they were cut into cubes (1 mm × 1 mm × 1 mm) and converge-milled. [35] The small particles were rotated with high-carbon chromium steel balls (JIS SUJ2/ASTM A295 52100: 8 mm ϕ) at 600 rpm for 5 h under an Ar atmosphere in a chamber, in which they were hurled toward a wall by a guide vane and toward an impact area and crashed into the wall. [35] This converge-milling process can apply heavy deformation to a sample. [35]

Thermodynamic calculations were performed using Thermo-Calc software [36] with the TCHEA2 database (Thermo-Calc Software AB).

3 Results

3.1 Phase Equilibria

The phase equilibria of the three Fe-Cr-Co-20Mn alloys at 1300 °C were investigated. Figure 2 shows the back-

scattered electron (BSE) image of the $\alpha + \gamma$ two-phase microstructure of the 37.6Fe-22.4Cr-20Co-20Mn alloy annealed at 1300 °C for 24 h. Table 1 shows the chemical compositions of the three alloys. Fe and Co are more strongly concentrated in the γ phase, while Cr segregates to the α phase. Mn is almost equally partitioned into the α and γ phases. Therefore, the equilibrium compositions are plotted in the isothermal diagram at the 20 at.% Mn section at 1300 °C, as shown in Fig. 1, where the solid lines denote the phase boundaries based on the experimental results of the phase equilibria. The phase boundaries calculated using the TCHEA2 database are denoted by dashed lines. The $\alpha + \gamma$ two-phase region is wider than the experimentally determined region by a few at.%, but the difference is within a limited range. Similar to the Fe-Cr-Co ternary system, the α and γ solid solutions formed in the Cr-rich and Cr-poor regions, respectively, in a wide composition range,^[27, 28] and the Gibbs energy of each phase crossed in the middle. We investigated the phase transformation, focusing on the composition range near the phase boundaries.

3.2 $\gamma \rightarrow \varepsilon$ Transformation

The phase transformation from the γ single-phase region at 1300 °C (Fig. 2) was examined. Figure 3(a) depicts the optical micrograph of the 48Fe-16Co-16Cr-20Mn alloy quenched at 1300 °C, and its TEM bright-field image with the selected area diffraction pattern (SADP) reveals ε martensite with stacking faults in the γ matrix (Fig. 3(b)). The orientation relationship is the Shoji-Nishiyama relationship: $(111)_\gamma // (0001)_\varepsilon$, $[\bar{1}10]_\gamma // [11\bar{2}0]_\varepsilon$. It is well known that Fe-Mn alloys exhibit a $\gamma \rightarrow \varepsilon$ martensitic transformation, and that the addition of Cr and Co slightly

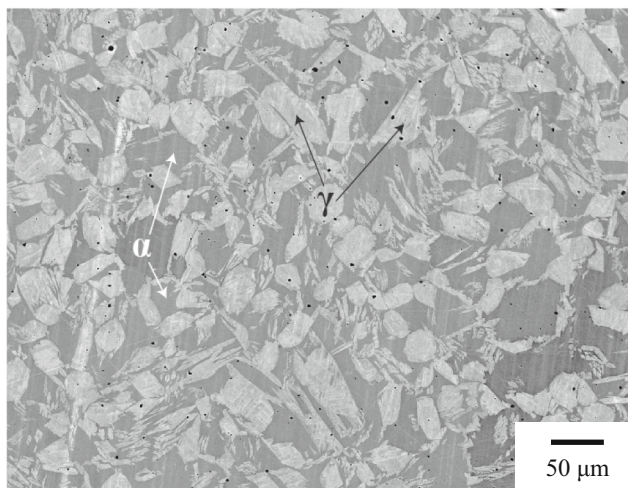


Fig. 2 BSE image of 37.6Fe-22.4Cr-20Co-20Mn alloy annealed at 1300 °C for 24 h

decreases the martensitic transformation temperature in the Fe-Mn-Cr^[37, 38] and Fe-Mn-Co^[39] ternary alloys. Co-Cr alloys exhibit the same type of transformation, in which the addition of Cr increases the martensitic transformation temperature.^[34] Moreover, the relative stability between the γ and ε phases has been investigated in (60-x)Fe-30Mn-10Cr-xCo (x = 0-12.5) quaternary alloys.^[40] They show that the $\gamma \rightarrow \varepsilon$ martensitic transformation, and M_s increases with increasing Co content. It has also been reported that the 50Fe-30Mn-10Co-10Cr alloy has an ε phase, resulting in high strength and high ductility.^[14] Our results reveal that Fe-Mn-based alloys with lower Mn and higher Co and Cr contents can exhibit the $\gamma \rightarrow \varepsilon$ martensitic transformation, which might provide valuable information for the alloy design of high-toughness HEAs.

3.3 $\alpha \rightarrow \varepsilon$ Transformation

The phase transformation from the α -single-phase region at 1300 °C was examined. Figure 4(a) and (b) depicts the optical micrographs of the 40.5Fe-27Cr-22.5Co-10Mn and 36Fe-24Cr-20Co-20Mn (Alloy A) alloys with the same Fe:Cr:Co ratio (45:30:25) quenched at 1300 °C, respectively. The 10Mn alloy (Fig. 4(a)) contained an α phase, whereas plate products were observed in the 20Mn alloy (Fig. 4(b)). Figure 4(c) exhibits a higher fraction of the plate phase in the 35.6Fe-24Cr-20.4Co-20Mn alloy (Alloy B) with a slightly higher Co content than Alloy A by substituting Fe. The TEM bright-field image and corresponding SADP of Alloy B are shown in Fig. 5. The plate phase was identified as martensite containing a high density of stacking faults with the HCP structure (ε phase) transformed from the BCC α phase, exhibiting a Burgers orientation relationship: $(110)_\alpha // (0002)_\varepsilon$, $[\bar{1}11]_\alpha // [11\bar{2}0]_\varepsilon$. Therefore, Fig. 4(a) and (b) infers that Mn stabilizes the ε phase and that the $\alpha \rightarrow \varepsilon$ martensitic transformation occurs during cooling in the Fe-Cr-Co-Mn system. Figure 4(d) shows the microstructure of the 35.2Fe-24.8Cr-20Co-20Mn alloy (Alloy C) with a higher Cr content than Alloy A by substituting Fe. The martensite phase was not observed, but the α single phase was observed. Compared to the martensitic transformation from the γ parent to ε in the Fe-Mn and Co alloys, the transformation from the α parent to ε is very rare in any combination of the constituting elements.

This martensitic transformation is partial, and the retained α -parent phase is observed. Therefore, Alloy B was cooled by liquid nitrogen, and the microstructure was observed. Surprisingly, the martensitic transformation did not proceed by sub-zero cooling, as shown in Fig. 4(e) and (f), which will be discussed in Sect. 4.

Table 1 Equilibrium compositions between α and γ phases in Fe-Cr-Co-Mn alloys at 1300 °C

Nominal alloy composition, at.%	Equilibrium composition, at.%							
	α (BCC)				γ (FCC)			
	Fe	Cr	Co	Mn	Fe	Cr	Co	Mn
Fe-20Cr-20Co-20Mn	39.5	22.0	19.1	19.4	40.7	18.8	21.1	19.4
Fe-22.4Cr-20Cr-20Mn	37.4	23.1	19.9	19.6	38.4	20.0	22.0	19.6
Fe-24Cr-21.6Co-20Mn	34.2	24.6	21.6	19.6	35.3	21.2	23.9	19.6

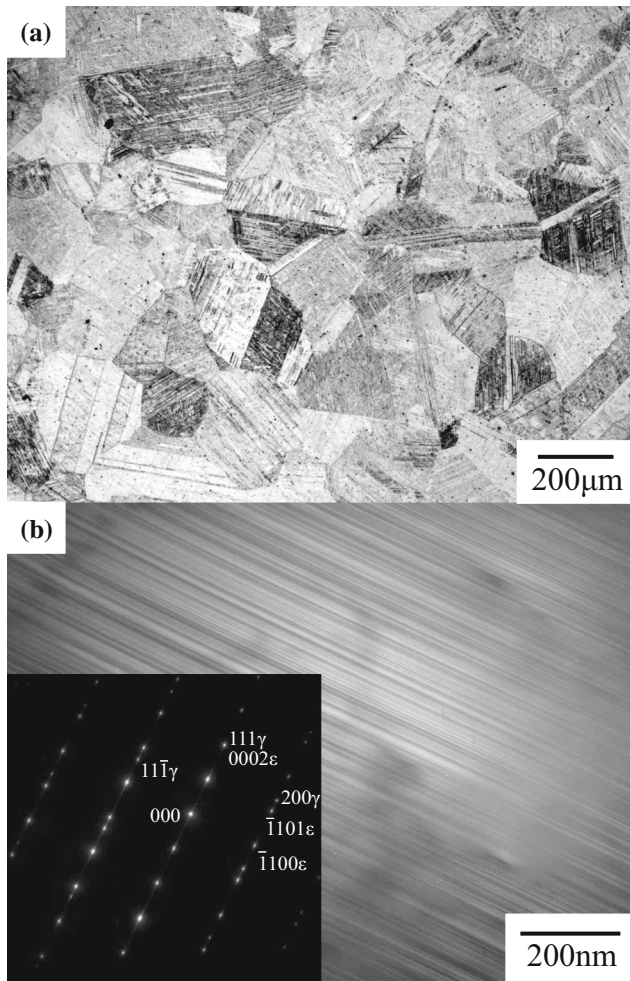


Fig. 3 (a) Optical micrograph of ε martensite transformed from the γ phase. (b) TEM bright-field image with selected area diffraction pattern of the 48Fe-16Cr-16Co-20Mn alloy. The incident beam direction is $[\bar{1}10]_{\gamma}$ and $[11\bar{2}]_{\varepsilon}$

The results for the martensitic transformation are indicated by different symbols in Fig. 1. It is inferred that Co stabilizes the ε phase, but Cr destabilizes the ε phase relative to the α phase. The relative stabilities of the α and ε phases in Fe have been reported as follows: ^[41] Mn strongly stabilizes the ε phase, and Cr is also an ε -stabilizing element in Fe, while Co is an α -stabilizing element. The results in the present study are different from those for Fe. However, the Fe-Cr-Co-Mn alloys are multi-

component, and thus we need to consider the interactions in many kinds of atom pairs, as well as the change in the surface of reference for Gibbs energy and configurational entropy, which is not so simple. Therefore, the phase stability between the α and ε phases was analyzed using the CALPHAD method and will be discussed in Sect. 4.

3.4 Bainitic Transformation

The Fe-24Cr-20Mn-20Mn alloy (Alloy A) was aged at 200 °C, 300 °C, and 400 °C for 24 h; the optical micrographs are shown in Fig. 6. This alloy exhibits the $\alpha \rightarrow \varepsilon$ martensitic transformation shown as thick white plates in Figs. 4(b) and 6(a), and thin plates are observed after aging at 200 °C in the matrix in Fig. 6(a). The fraction of the thin plates increased with increasing aging temperature (Fig. 6(a)-(c)), and the hardness increased from ~250 HV to 400 HV by increasing the aging temperature from 200 to 400 °C (Fig. 6(d)). This is not a feature of martensite, and we further investigated this phase using TEM. The optical micrograph and TEM bright-field image with SADP of as-quenched 34.4Fe-24.8Cr-20.8Co-20Mn are shown in Fig. 7(a) and (b), respectively. Similar thin plates, in addition to the thick martensite plates, are observed in Fig. 7(a). As shown in Fig. 7(b), the width of the plate is approximately 250 nm, which is considerably thinner than that of ε martensite, and it contains defects. The SADP indicates that this plate has a 6M structure. Based on the morphology, aging-induced transformation, and hardening, thin plates are presumably obtained by a bainitic transformation. The microstructure and crystal structure are similar to those in the early stage bainite (6M, 9R) in Cu-Zn and Cu-Al-Mn alloys. ^[42-48]

3.5 $\alpha \rightarrow \varepsilon \rightarrow \gamma$ Transformations

Cold rolling was applied to 35.6Fe-24Cr-20.4Co-20Mn (Alloy B) to further induce the ε martensite phase. The XRD results show that the as-quenched specimen has ε martensite with a retained α parent phase (Fig. 8(a)), which is consistent with Fig. 5. Further, an almost full ε martensite phase was obtained after 50% cold rolling

Fig. 4 Optical micrographs of (a) 40.5Fe-27Cr-22.5Co-10Mn, (b) 36Fe-24Cr-20Co-20Mn (Alloy A), (c) 35.6Fe-24Cr-20.4Co-20Mn (Alloy B), and (d) 35.2Fe-24.8Cr-20Co-20Mn (Alloy C) alloys annealed at 1300 °C for 30 min. Optical micrographs of Alloy B (e) before and (f) after sub-zero treatment using liquid nitrogen

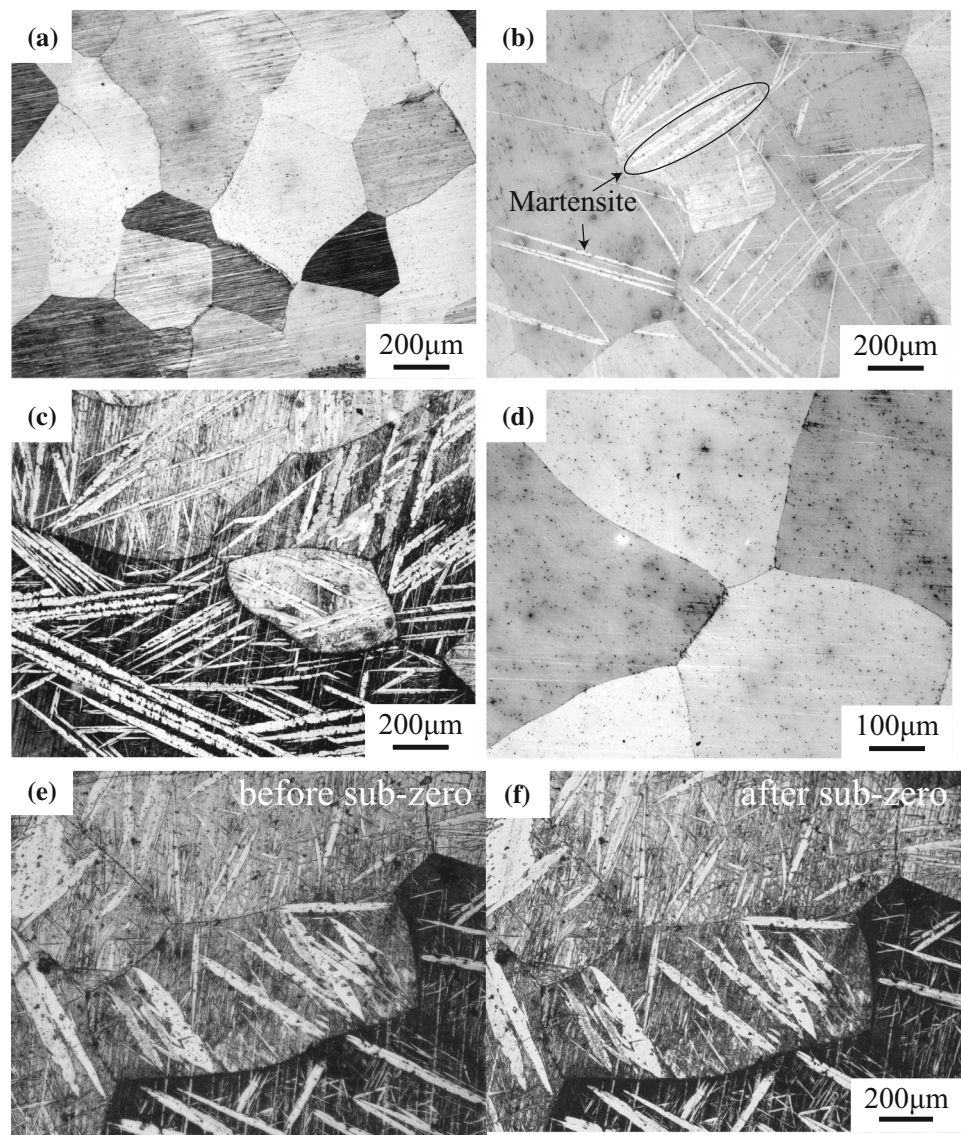


(Fig. 8(b)). Therefore, it can be concluded that the $\alpha \rightarrow \varepsilon$ martensitic transformation was induced by cold rolling.

Heavy deformation was applied to Alloy B by converge-milling. The XRD profiles before and after converge-milling are shown in Fig. 8(c) and (d), respectively. The as-quenched particles have α and ε phases, similar to Fig. 8(a), but the fraction of the ε phase is drastically decreased and the γ phase is induced by converge-milling. This result indicates that both the $\alpha \rightarrow \varepsilon$ and $\varepsilon \rightarrow \gamma$ transformations were induced by heavy deformation, which is probably a martensitic transformation. These results showed that multiple martensitic transformations of $\alpha \rightarrow \varepsilon$ by cooling or deformation and $\varepsilon \rightarrow \gamma$ by deformation occurred in this system. Interestingly, the present alloy exhibits a path the opposite to that of the $\gamma \rightarrow \varepsilon \rightarrow \alpha'$ (BCC) martensitic transformations in Fe-Cr-Ni^[49-52] and Fe-Mn^[53-55] alloys.

The lattice parameters of the α , ε , and γ phases were determined by XRD experiments and are listed in Table 2. The volume change from α to ε is -2.39% , whereas that from ε to γ is close to zero.

Magnetization was measured at room temperature and the results are shown in Fig. 9. The as-quenched sample with the α parent and ε martensite phases showed high magnetization of ~ 100 emu/g. However, the magnetization reduced to approximately 20 emu/g in the ε martensite phase induced by 50% cold rolling. The γ martensite phase induced by converge-milling with a smaller amount of retained ε and α phases also exhibited a lower magnetization of ~ 30 emu/g. The magnetic phase diagrams of BCC $(80-x)\text{Cr}-20\text{Fe}-x\text{Mn}$ and $(75-x)\text{Cr}-25\text{Fe}-x\text{Mn}$ have been reported, and these alloys were ferromagnetic, anti-ferromagnetic, or spin glass depending on the composition and temperature.^[56, 57] The Curie temperature increased to

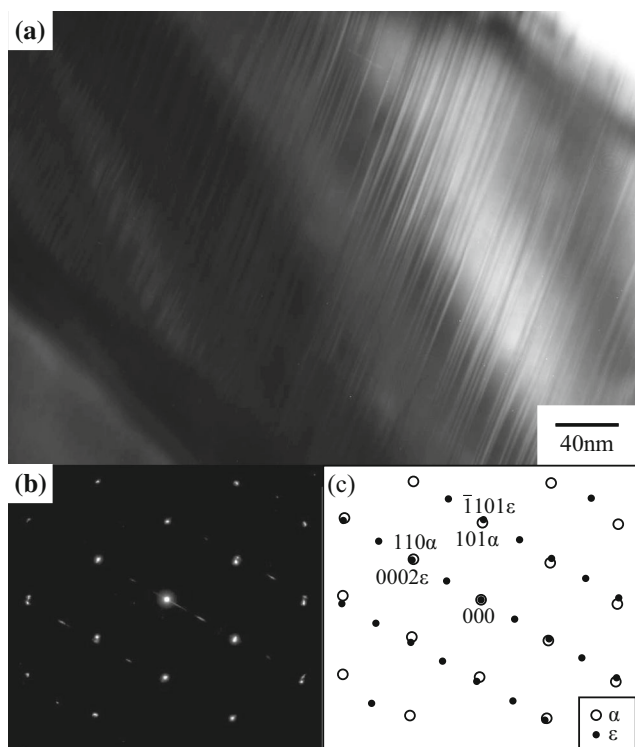


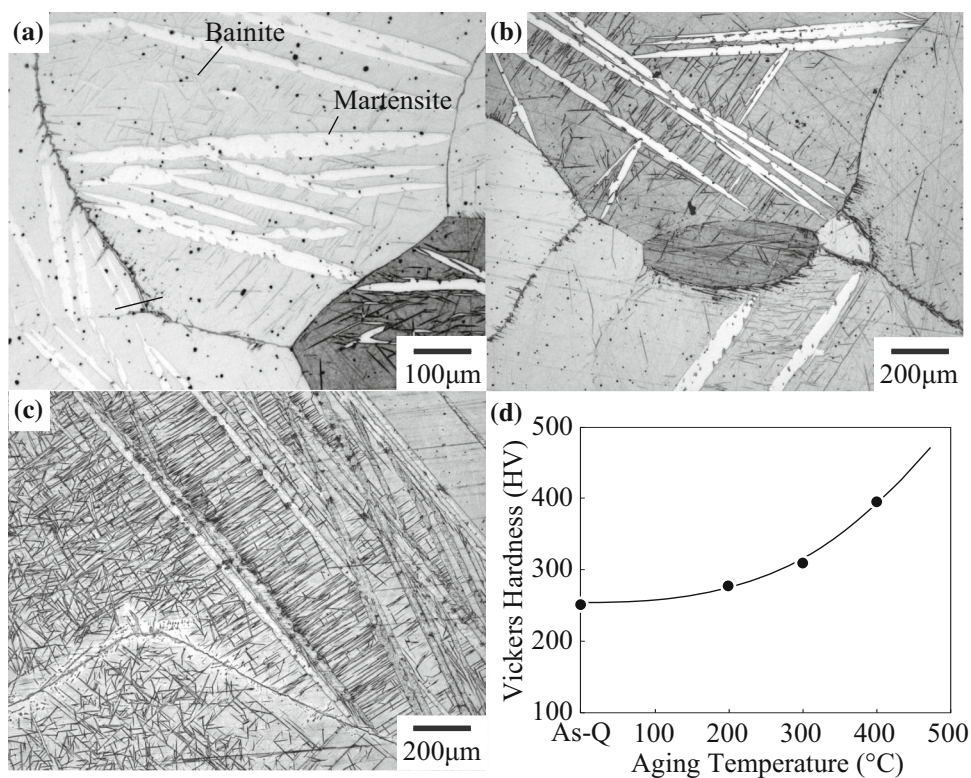
Fig. 5 (a) TEM bright-field image of ε martensite, (b) selected area diffraction pattern, and (c) its key diagram of 35.6Fe-24Cr-20.4Co-20Mn (Alloy B). The incident beam directions are $[\bar{1}11]\alpha$ and $[11\bar{2}0]\varepsilon$

approximately -70 °C upon increasing the Fe content to 25%. In the present study, the α phase was ferromagnetic at room temperature, which was due to the higher Fe content. Magnetism can affect phase stability, as discussed in the next section.

4 Discussion

Here, the martensitic phase transformation is discussed based on the Gibbs energy of each phase. The calculated Gibbs energy difference, $\Delta G_m^{\alpha/\varphi} = G_m^\varphi - G_m^\alpha$ (φ : ε or γ) in Fe-24Cr-20Co-20Mn (Alloy A) is illustrated in Fig. 10 as a function of the temperature. The calculated Gibbs energy curves of the α , ε , and γ phases at temperatures between 200 and 1300 °C in the Fe-Cr-20Co-20Mn section are shown in Fig. 11. First, the phase stability between the α and ε phases is discussed. Figure 10 shows that $\Delta G_m^{\alpha/\varepsilon}$ remained positive over the entire temperature range, indicating that the α phase is more stable than the ε phase. However, Figs. 4 and 5 show that the experiments in this study revealed the $\alpha \rightarrow \varepsilon$ transformation on cooling. Furthermore, the $\gamma \rightarrow \varepsilon$ transformation in the 48Fe-16Co-16Cr-20Mn alloy could not be explained by the calculation. These contradictions are resolved by the stabilization of ε

Fig. 6 Optical micrographs of 36Fe-24Cr-20Co-20Mn (Alloy A) aged at (a) 200 °C, (b) 300 °C, and (c) 400 °C for 24 h. (d) Vickers hardness against aging temperature in Alloy A aged for 24 h



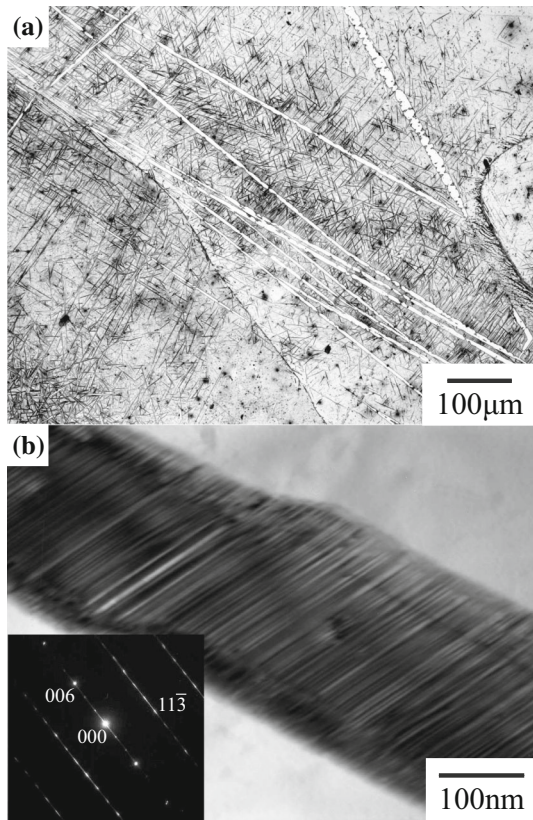


Fig. 7 Microstructure of as-quenched 34.4Fe-24.8Cr-20.8Co-20Mn: (a) optical micrograph, and (b) bright-field image with selected area diffraction pattern. The incident beam direction is $[1\bar{1}0]_{6M}$

by 1 kJ/mol independent of temperature (denoted as $G_m^{\varepsilon(-1k)}$) in the calculation. The ε phase becomes more stable at temperatures between 94 and 575 °C, which are $T_0^{\alpha/\varepsilon(-1k)}$ points. In the isoplethal section of Fe-Cr-20Co-20Mn in Fig. 11, the $T_0^{\alpha/\varepsilon(-1k)}$ points are indicated by filled circles. Although G_m^ε is higher than G_m^α at any Cr content at 200–1300 °C, $G_m^{\varepsilon(-1k)}$ intersects with G_m^α at 600 °C and lower temperatures; thus, $T_0^{\alpha/\varepsilon(-1k)}$ exists. The $T_0^{\alpha/\varepsilon}$ and $T_0^{\alpha/\varepsilon(-1k)}$ lines are illustrated in the same Fe-Cr-20Co-20Mn section in Fig. 12(a) and (b), respectively. In Fig. 12(a), the 24Cr alloy does not cross the $T_0^{\alpha/\varepsilon}$ line, which disagrees with the experimental result of the $\alpha \rightarrow \varepsilon$ martensitic transformation, and $T_0^{\alpha/\varepsilon}$ is only observed at high Cr contents. In contrast, Fig. 12(b) shows that the $T_0^{\alpha/\varepsilon(-1k)}$ the 24Cr alloy occurs at 575 °C, and the $\gamma \rightarrow \varepsilon$ martensitic transformation seems to occur as shown in the $T_0^{\gamma/\varepsilon(-1k)}$ line, unlike the $T_0^{\gamma/\varepsilon}$ line. Therefore, the ε phase should be more stable than the thermodynamic parameters assessed in TCHEA2.

As shown in Fig. 10, the ε phase stabilized by 1 kJ/mol is more stable than the α phase at temperatures lower than

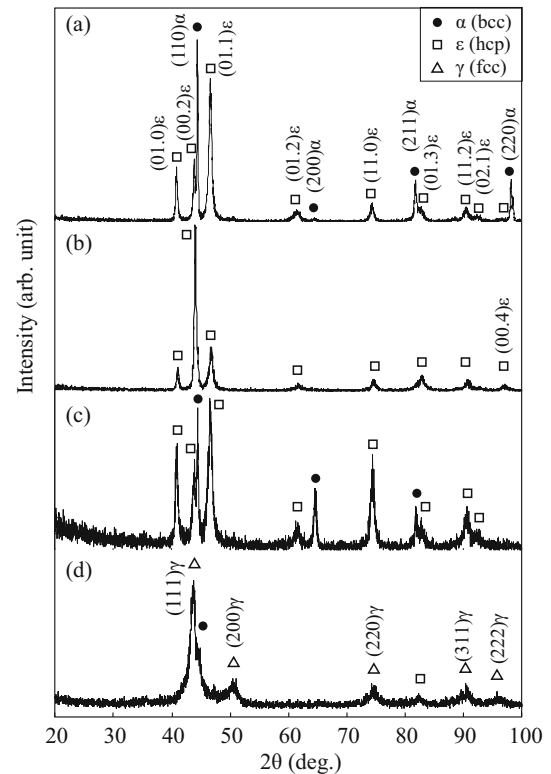


Fig. 8 XRD patterns of 35.6Fe-24Cr-20.4Co-20Mn (Alloy B): (a) as-quenched sheet, (b) 50% cold-rolled sheet, (c) as-quenched particles, and (d) converge-milled particles.

575 °C and the α phase appears to be stabilized again by further cooling, crossing $G_m^{\varepsilon(-1k)}=0$ at 94 °C. In the vertical section diagram of Fig. 12(b), the dependence of the $T_0^{\alpha/\varepsilon(-1k)}$ line on the Cr content is weak, being almost constant at approximately 600 °C, while the $T_0^{\alpha/\varepsilon(-1k)}$ line abruptly bends around 15Cr and 450 °C. This peculiar behavior is discussed next.

As shown in Fig. 10, the γ phase becomes more stable relative to the α phase at 1148 °C during cooling, suggesting the possibility of martensitic transformation from α to γ . However, γ martensite was not observed in 24Cr (Alloy A) in the experiments. Therefore, this prediction from the thermodynamic calculation might be incorrect because of the lack of accuracy in the Gibbs energy of the α and/or γ phases. Another possible reason is the increase in $\Delta G_m^{\alpha/\gamma}$ upon further cooling. Martensitic transformation can be induced when the chemical Gibbs energy difference overcomes the non-chemical contribution below the T_0 temperature, including plastic deformation, elastic strain, and interface. The $\Delta G_m^{\alpha/\gamma}$ obtained by cooling may be insufficient because of the increase in $G_m^{\alpha/\gamma}$ upon cooling in this alloy. This behavior is caused by the magnetic transition of the α phase. The calculated Curie temperature T_C^α is 326 °C, which is consistent with the

Table 2 Lattice parameters of α , ε , and γ phases in 35.6Fe-24Cr-20.4Co-20Mn (Alloy B)

Condition	Phase	Lattice parameter, nm			Volume change ΔV , %
		a	c	c/a	
As-Quenched	α (BCC)	0.2882			
As-Quenched	ε (HCP)	0.2555	0.4133	1.618	- 2.39 ($\alpha \rightarrow \varepsilon$)
Converge Milled	γ (FCC)	0.3603			0.0887 ($\varepsilon \rightarrow \gamma$)

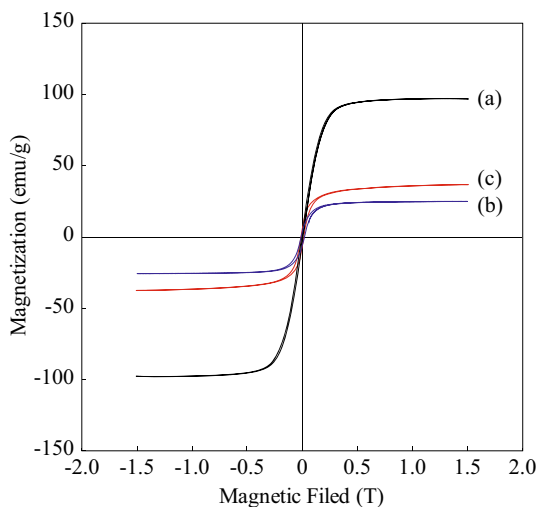


Fig. 9 Magnetization curves of 35.6Fe-24Cr-20.4Co-20Mn (Alloy B): (a) as-quenched sheet, (b) 50% cold-rolled sheet, and (c) converge-milled powders

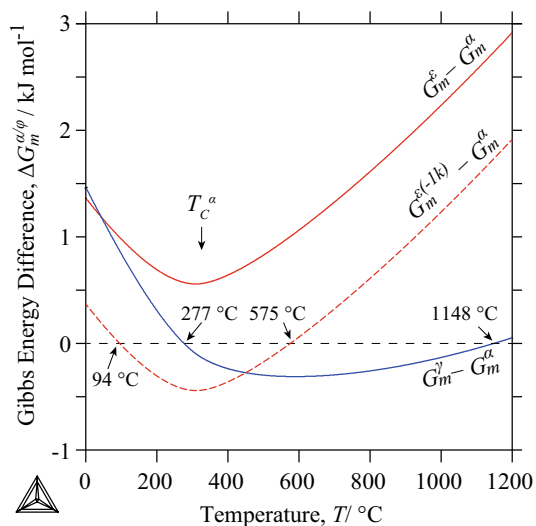


Fig. 10 Calculated Gibbs energy/temperature curves of ε , ε added - 1 kJ/mol, and γ phases relative to that of the α phase in Fe-24Cr-20Co-20Mn (Alloy A). The calculated Curie temperature of α phase T_C^α is also indicated.

ferromagnetic feature in the magnetization curve of the quenched sample at room temperature, as shown in Fig. 9. The magnetic ordering reduces the entropy S_m^α on cooling from the paramagnetic reference state at high temperatures.

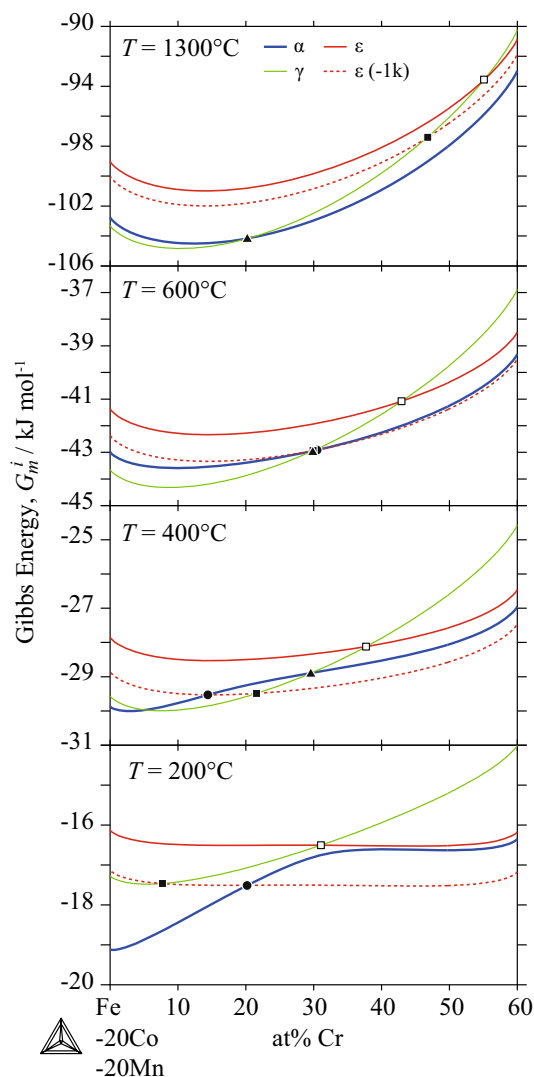


Fig. 11 Calculated Gibbs energy of α , ε , ε' , and γ phases at 1300 °C, 600 °C, 400 °C, and 200 °C in Fe-Cr-20Co-20Mn section.

Thus, $\Delta S_m^{\alpha/\gamma} = S_m^\gamma - S_m^\alpha$ increases, resulting in the stabilization of the α phase upon cooling. The α phase is even more stable than the γ phase at temperatures below 277 °C, as shown in Fig. 10. The effect of magnetism of the α phase is shown in Fig. 13(a) and (c), where the Gibbs energy of the α phase is expressed as $G_{total}^\alpha = G_{nonmag}^\alpha + G_{mag}^\alpha$. The magnetic transition on the phase stability of Fe and Fe alloys exhibits a similar effect. [26, 58-61]

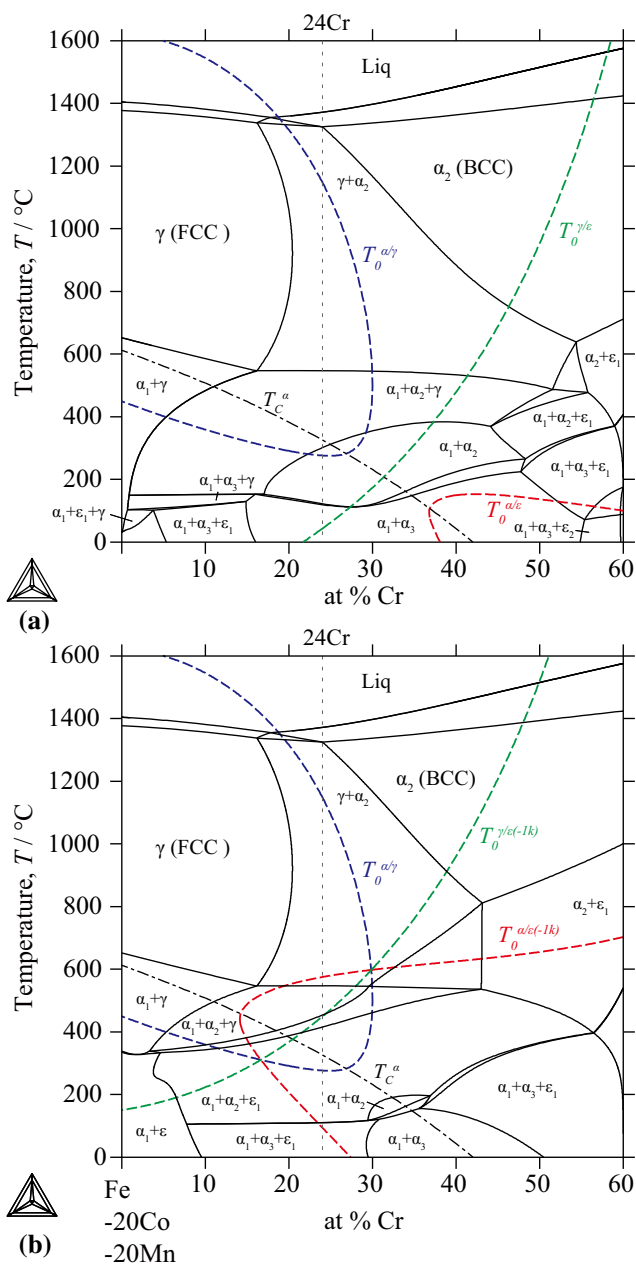


Fig. 12 (a) Calculated vertical section diagram in the Fe-Cr-20Co-20Mn section with T_0 lines between α and γ phases, α and ϵ phases, and γ and ϵ phases. (b) Same as (a) but ϵ is replaced by ϵ stabilized by 1 kJ/mol in the calculation. Subscript α and ϵ indicates phase separation (α_1 : Fe-Co-rich BCC, α_2 : Cr-rich BCC, α_3 : Cr-rich BCC, ϵ_1 : Co-Mn-Cr-rich HCP, ϵ_2 : Co-rich HCP). α , ϵ , and γ phases were included in the calculation, whereas σ and other phases were excluded.

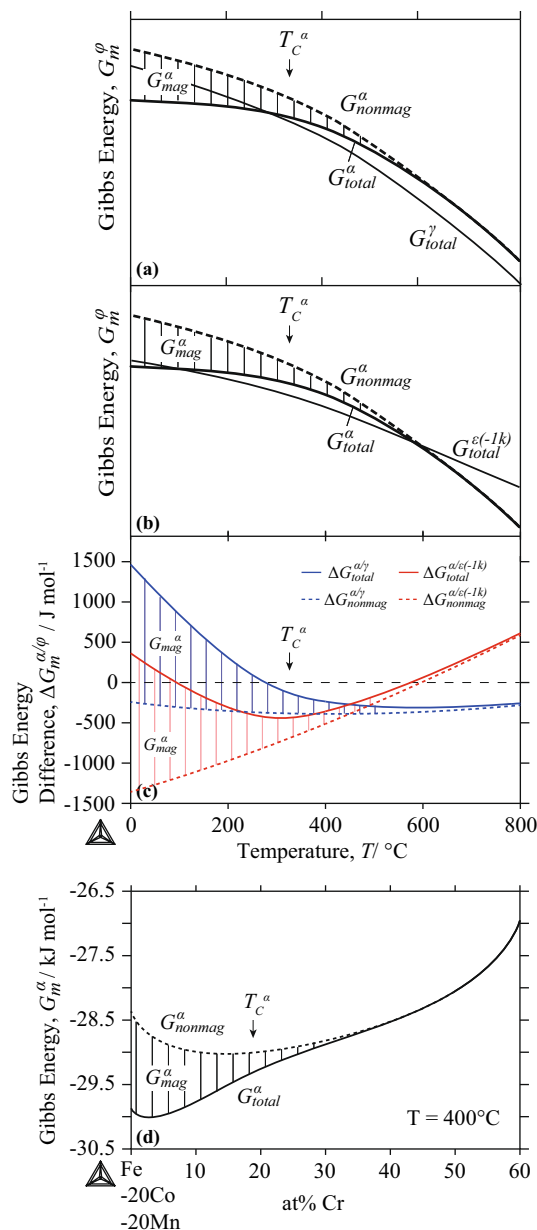


Fig. 13 Schematic illustrations of the Gibbs energy-temperature curves of (a) α and γ phases and (b) α and $\epsilon(-1k)$ phases. Calculated (c) Gibbs energy difference-temperature curves of ϵ and γ phases relative to the α phase in Fe-24Cr-20Co-20Mn (Alloy A) and (d) Gibbs energy-Cr content curves at 400 °C in Fe-Cr-20Co-20Mn. G_{total}^{ϕ} is divided into the nonmagnetic term, G_{nonmag}^{ϕ} , and magnetic contribution, G_{mag}^{ϕ} , to discuss magnetic effect. (a) and (b) Schematic diagrams showing the magnetic contribution instead of calculation. (c) and (d) Calculated diagrams using the TCHEA2 database.

The $T_0^{\alpha/\gamma}$ points of 24Cr are 1148 °C and 277 °C, as shown in Fig. 10. In the isoplethal section of Fe-Cr-20Co-20Mn in Fig. 11, the $T_0^{\alpha/\gamma}$ points are shown by triangles. The T_C^z line in this section (Fig. 12) decreases with increasing Cr content. The Cr content at which T_C^z is 400 °C is 18.7%. At 400 °C (Fig. 11), G_m^z is noticeably lowered at Cr contents lower than approximately 20%. This is caused by magnetic ordering, as discussed above and shown in Fig. 13(d). Since T_C^z decreases with increasing Cr content, a similar behavior can be observed from a higher Cr content at a lower temperature of 200 °C. The decrease in Gibbs energy in the ferromagnetic state results in a miscibility gap between the ferromagnetic and paramagnetic states, termed Nishizawa Horn, [32, 62, 63] which is observed in the present Fe-Cr-Co-Mn system.

The $T_0^{\alpha/\gamma}$, $T_0^{\alpha/\varepsilon}$, $T_0^{\alpha/\varepsilon(-1k)}$, and $T_0^{\gamma/\varepsilon}$ lines are illustrated in the vertical section at Fe-Cr-20Co-20Mn of the calculated phase diagram in Fig. 12. The phase stabilities of the α , $\varepsilon(-1k)$, and γ phases are close to each other near 36Fe-24Cr-20Co-20Mn; therefore, martensitic transformations can reasonably easily occur. The bainite formed at 200–400 °C has a 6M structure (Fig. 7), which is a mixture of the FCC and HCP stacking of the close-packed plane. [64] This fact may support the close stability of FCC- γ and HCP- ε in this composition and temperature region.

The $T_0^{\alpha/\gamma}$ line shows a loop in Fig. 12 because of the magnetic effect, and stabilization of the α phase is observed below the T_C^z temperature. This is similar to the γ loop in Fe alloys (e.g., the Fe-Cr system). [63, 65] Notably, one can also find a loop of $T_0^{\alpha/\varepsilon(-1k)}$, that is the ε loop. The origin of the ε loop is the same as that of the γ loop, namely the magnetic ordering in the α phase, as shown in Fig. 13(b) and (c). The ε loop indicates that, unlike usual martensitic transformations, the α parent phase is stabilized by cooling instead of increasing the driving force for the $\alpha \rightarrow \varepsilon$ martensitic transformation. This type of reentrant martensitic transformation has been observed in Co-based Heusler alloys. [66–68] Notably, ε martensite is partially induced by water quenching and the martensitic transformation does not occur by further cooling using liquid nitrogen in this system, as confirmed in Fig. 4(e) and (f), although aging at 200–400 °C induces bainite. These experimental results support the existence of an ε loop. The direction of the ε loop is opposite because the state in which the ε phase is more stable than the α phase exists on the Cr-rich side. This novel ε loop confirms the universal effect of magnetic ordering on the phase stability.

Finally, the T_0 lines in the other sections are discussed. The experimental results in Fig. 4(a)–(c) and summarized

in Fig. 1 imply that Cr stabilizes the α phase relative to the ε phase in the iso-Co (i.e., Fe/Cr substitution) and iso-Fe (i.e., Co/Cr substitution) sections, and that Co stabilizes the ε phase relative to the α phase in the iso-Cr (i.e., Fe/Co substitution) section, where Mn is constant. The $T_0^{\alpha/\varepsilon}$ line exhibits weak dependence on Cr content in the iso-Co section in Fig. 12, which does not correlate with the relative phase stability suggested by the experiments. The $T_0^{\alpha/\varepsilon}$ lines in the iso-Cr (24Cr) and iso-Fe (35Fe) sections are shown in Fig. 14. The trends for the relative α/ε phase stability depending on Co and Cr content in the calculations are consistent with those in the experiments. In these sections, the T_0 lines are influenced so that the ferromagnetic α phase is stabilized and ε loops with different shapes, as well as γ loops, are observed. The impact of magnetism was clearly observed.

5 Summary

The phase transformations and phase stability of the Fe-Cr-Co-Mn system were investigated through experiments and calculations. The phase transformation from the α phase with the BCC structure was examined around the 36Fe-24Cr-20Co-20Mn composition. Fe-Cr-Co-Mn alloys exhibited thermal martensitic transformation from the α phase to the ε phase with the HCP structure. The retained α parent phase was transformed to the ε phase by cold rolling, and the FCC-structured γ phase was induced by heavy deformation via converge-milling, implying the $\varepsilon \rightarrow \gamma$ martensitic transformation. Therefore, it can be concluded that multiple martensitic transformations $\alpha \rightarrow \varepsilon$ and $\varepsilon \rightarrow \gamma$ can occur in this system. The $\gamma \rightarrow \varepsilon$ martensitic transformation was also observed for 48Fe-16Cr-16Co-20Mn. These phase transformations can be utilized to enhance the mechanical properties of HEAs.

The Gibbs energy and T_0 lines were calculated to predict the martensitic transformation, and the phase stabilities of the α , ε , and γ phases were similar in this composition range. More specifically, the experimental results suggest that the ε phase is more stable than that assessed in the current database of the Fe-Cr-Co-Mn system. The thermodynamic calculation revealed that ferromagnetic ordering in the α phase affects the relative phase stability, resulting in the ε loop in addition to the conventional γ loop. The predicted relative phase stability of α/ε (or ε loop) was supported by the experimental results, which revealed that the $\alpha \rightarrow$ 6M bainitic transformation occurred by aging at 200–400 °C and $\alpha \rightarrow \varepsilon$ martensitic

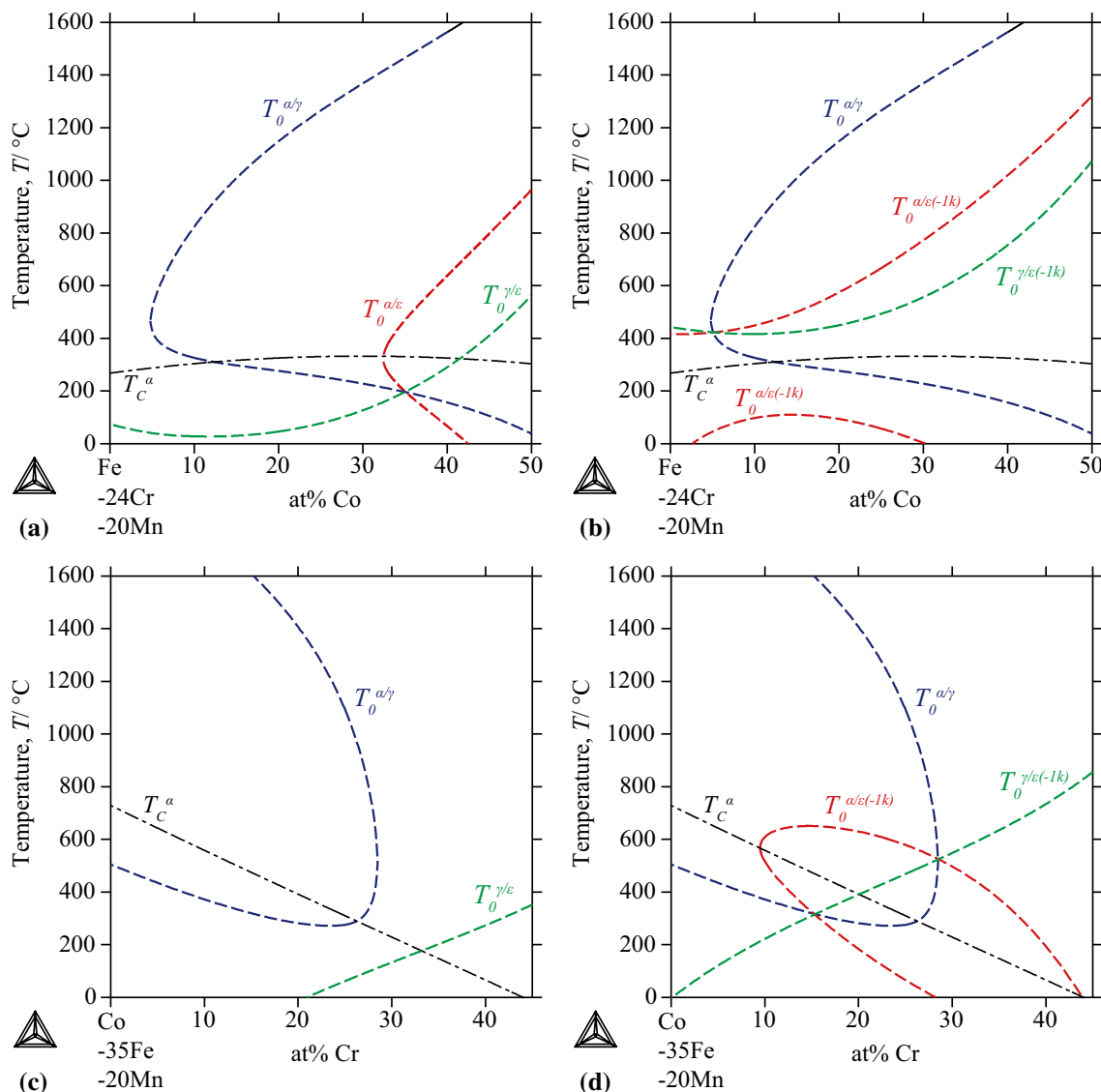


Fig. 14 Calculated T_0 lines between α and γ phases, α and ϵ phases, and γ and ϵ phases in (a) Fe-24Cr-Co-20Mn section and (c) 35Fe-Cr-Co-20Mn section. (b) and (d) Same as (a) and (c), respectively, but ϵ is replaced by ϵ stabilized by 1 kJ/mol.

transformation did not proceed by sub-zero treatment using liquid nitrogen.

References

1. J.W. Yeh, S.K. Chen, S.J. Lin, J.Y. Gan, T.S. Chin, T.T. Shun, C.H. Tsau, and S.Y. Chang, Nanostructured High-Entropy Alloys with Multiple Principal Elements: Novel Alloy Design Concepts and Outcomes, *Adv. Eng. Mater.*, 2004, **6**(5), p 299–303.
2. B. Cantor, I.T.H. Chang, P. Knight, and A.J.B. Vincent, Microstructural Development in Equiatomic Multicomponent Alloys, *Mater. Sci. Eng. A*, 2004, **375–377**, p 213–218.
3. M.-H. Tsai, and J.-W. Yeh, High-Entropy Alloys: A Critical Review, *Mater. Res. Lett.*, 2014, **2**(3), p 107–123.
4. Y. Zhang, T.T. Zuo, Z. Tang, M.C. Gao, K.A. Dahmen, P.K. Liaw, and Z.P. Lu, Microstructures and Properties of High-Entropy Alloys, *Prog. Mater. Sci.*, 2014, **61**, p 1–93.
5. D.B. Miracle, and O.N. Senkov, A Critical Review of High Entropy Alloys and Related Concepts, *Acta Mater.*, 2017, **122**, p 448–511.
6. A. Gali, and E.P. George, Tensile Properties of High- and Medium-Entropy Alloys, *Intermetallics*, 2013, **39**, p 74–78.
7. F. Otto, A. Dlouhý, C. Somsen, H. Bei, G. Eggeler, and E.P. George, The Influences of Temperature and Microstructure on the Tensile Properties of a CoCrFeMnNi High-Entropy Alloy, *Acta Mater.*, 2013, **61**(15), p 5743–5755.
8. M. Kawamura, M. Asakura, N.L. Okamoto, K. Kishida, H. Inui, and E.P. George, Plastic Deformation of Single Crystals of the Equiatomic Cr–Mn–Fe–Co–Ni High-Entropy Alloy in Tension and Compression from 10 K to 1273 K, *Acta Mater.*, 2021, **203**, p 116454.
9. B. Gludovatz, A. Hohenwarter, D. Catoor, E.H. Chang, E.P. George, and R.O. Ritchie, A Fracture-Resistant High-Entropy

- Alloy for Cryogenic Applications, *Science*, 2014, **345**(6201), p 1153–1158.
10. C.Y. Hsu, C.C. Juan, W.R. Wang, T.S. Sheu, J.W. Yeh, and S.K. Chen, On the Superior Hot Hardness and Softening Resistance of AlCoCrFeMo05Ni High-Entropy Alloys, *Mater. Sci. Eng. A-Struct. Mater. Prop. Microstruct. Process.*, 2011, **528**(10–11), p 3581–3588.
 11. O.N. Senkov, S.V. Senkova, D.B. Miracle, and C. Woodward, Mechanical Properties of Low-Density, Refractory Multi-Principal Element Alloys of the Cr–Nb–Ti–V–Zr System, *Mater. Sci. Eng. A*, 2013, **565**, p 51–62.
 12. F. Maresca, and W.A. Curtin, Mechanistic Origin of High Strength in Refractory BCC High Entropy Alloys up to 1900K, *Acta Mater.*, 2020, **182**, p 235–249.
 13. M.-H. Tsai, Physical Properties of High Entropy Alloys, *Entropy*, 2013, **15**(12), p 5338–5345.
 14. Z. Li, K.G. Pradeep, Y. Deng, D. Raabe, and C.C. Tasan, Metastable High-Entropy Dual-Phase Alloys Overcome the Strength-Ductility Trade-off, *Nature*, 2016, **534**(7606), p 227–230.
 15. K. Niitsu, M. Asakura, K. Yuge, and H. Inui, Prediction of Face-Centered Cubic Single-Phase Formation for Non-Equiatomic Cr–Mn–Fe–Co–Ni High-Entropy Alloys Using Valence Electron Concentration and Mean-Square Atomic Displacement, *Mater. Trans.*, 2020, **61**(9), p 1874–1880.
 16. J.-W. Yeh, Alloy Design Strategies and Future Trends in High-Entropy Alloys, *Jom*, 2013, **65**(12), p 1759–1771.
 17. C.-J. Tong, M.-R. Chen, J.-W. Yeh, S.-J. Lin, S.-K. Chen, T.-T. Shun, and S.-Y. Chang, Mechanical Performance of the Alx-CoCrCuFeNi High-Entropy Alloy System with Multiprincipal Elements, *Metall. Mater. Trans. A.*, 2005, **36**(5), p 1263–1271.
 18. X.F. Wang, Y. Zhang, Y. Qiao, and G.L. Chen, Novel Microstructure and Properties of Multicomponent CoCrCuFeNi-Tix Alloys, *Intermetallics*, 2007, **15**(3), p 357–362.
 19. J.M. Zhu, H.M. Fu, H.F. Zhang, A.M. Wang, H. Li, and Z.Q. Hu, Microstructures and Compressive Properties of Multicomponent AlCoCrFeNiMox Alloys, *Mater. Sci. Eng. A*, 2010, **527**(26), p 6975–6979.
 20. S. Singh, N. Wanderka, B.S. Murty, U. Glatzel, and J. Banhart, Decomposition in Multi-Component AlCoCrCuFeNi High-Entropy Alloy, *Acta Mater.*, 2011, **59**(1), p 182–190.
 21. C. Zhang, F. Zhang, S. Chen, and W. Cao, Computational Thermodynamics Aided High-Entropy Alloy Design, *Jom*, 2012, **64**(7), p 839–845.
 22. F. Zhang, C. Zhang, S.L. Chen, J. Zhu, W.S. Cao, and U.R. Kattner, An Understanding of High Entropy Alloys from Phase Diagram Calculations, *Calphad*, 2014, **45**, p 1–10.
 23. H. Mao, H.-L. Chen, and Q. Chen, TCHEA1: A Thermodynamic Database Not Limited for “High Entropy” Alloys, *J. Phase Equilib. Diffus.*, 2017, **38**(4), p 353–368.
 24. H.-L. Chen, H. Mao, and Q. Chen, Database Development and Calphad Calculations for High Entropy Alloys: Challenges, Strategies, and Tips, *Mater. Chem. Phys.*, 2018, **210**, p 279–290.
 25. H. Okamoto, Desk Handbook Phase Diagrams for Binary Alloys, 2nd edn. (ASM International, 2010)
 26. C. Zener, Impact of Magnetism Upon Metallurgy, *Trans. Am. Inst. Min. Metall. Eng.*, 1955, **203**(5), p 619–630.
 27. C. Allibert, C. Bernard, G. Effenberg, H.D. Nüssler, and P.J. Spencer, A Thermodynamic Evaluation of the FeCoCr System, *Calphad*, 1981, **5**(4), p 227–237.
 28. M. Dombre, O. Silva Campos, N. Valignat, C. Allibert, C. Bernard, and J. Driole, Solid State Phase Equilibrium in the Ternary Fe-Co-Cr System: Experimental Determination of Isothermal Sections in the Temperature Range 800–1300 °C, *J. Less Common Met.*, 1979, **66**(1), p 1–11.
 29. M. Okada, G. Thomas, M. Homma, and H. Kaneko, Microstructure and Magnetic Properties of Fe-Cr-Co Alloys, *IEEE Trans. Magn.*, 1978, **14**(4), p 245–252.
 30. H. Kaneko, M. Homma, K. Nakamura, M. Okada, and G. Thomas, Phase Diagram of Fe-Cr-Co Permanent Magnet System, *IEEE Trans. Magn.*, 1977, **13**(5), p 1325–1327.
 31. M. Homma, M. Okada, T. Minowa, and E. Horikoshi, Fe-Cr-Co Permanent Magnet Alloys Heat-Treated in the Ridge Region of the Miscibility Gap, *IEEE Trans. Magn.*, 1981, **17**(6), p 3473–3478.
 32. T. Nishizawa, M. Hasebe, and M. Ko, Thermodynamic Analysis of Solubility and Miscibility Gap in Ferromagnetic Alpha Iron Alloys, *Acta Metall.*, 1979, **27**(5), p 817–828.
 33. H. Masumoto, On the Thermal Expansion of Alloys of Cobalt, Iron and Chromium, and a New Alloy “Stainless-Invar” & “Stainless-Invar”, *J. Jpn. Inst. Met.*, 1938, **2**(4), p 141–146.
 34. J.C. Zhao, The fcc/hcp Phase Equilibria and Phase Transformation in Cobalt-Based Binary Systems, *Z. Fur Metallkunde*, 1999, **90**(3), p 223–232.
 35. I. Ohnuma, S. Shimenouchi, T. Omori, K. Ishida, and R. Kainuma, Experimental Determination and Thermodynamic Evaluation of Low-Temperature Phase Equilibria in the Fe-Ni Binary System, *Calphad-Comput. Coupling Ph. Diagr. Thermochem.*, 2019, **67**, p 101677.
 36. B. Sundman, B. Jansson, and J.-O. Andersson, The Thermo-Calc Databank System, *Calphad*, 1985, **9**(2), p 153–190.
 37. L.M. Guerrero, P. La Roca, F. Malamud, A. Baruj, and M. Sade, Composition Effects on the fcc-hcp Martensitic Transformation and on the Magnetic Ordering of the fcc Structure in Fe-Mn-Cr Alloys, *Mater. Des.*, 2017, **116**, p 127–135.
 38. L.M. Guerrero, P. La Roca, F. Malamud, A. Baruj, and M. Sade, A Short Review on the Effect of Cr on the fcc-hcp Phase Transition in Fe-Mn-Based Alloys, *Shape Memory Superelasticity*, 2020, **6**(2), p 202–212.
 39. A. Baruj, A.F. Guillermet, and M. Sade, The fcc/hcp Relative Phase Stability in the Fe-Mn-Co System: Martensitic Transformation Temperatures, Assessment of Gibbs Energies And Thermodynamic Calculation of T-0 Lines, *J. Phys. IV*, 1997, **7**(C5), p 405–410.
 40. M.D. Acciarri, P. La Roca, L.M. Guerrero, A. Baruj, J. Curiale, and M. Sade, Effect of FCC Anti-Ferromagnetic Ordering on the Stability of Phases in Fe60-xMn30Cr10Cox High Entropy Alloys, *J. Alloys Compd*, 2020, **823**, p 153845.
 41. K. Ishida, and T. Nishizawa, Effect of Alloying Elements on Stability of Epsilon Iron, *Trans. Jpn Inst. Metals*, 1974, **15**(3), p 225–231.
 42. T. Tadaki, C.J. Qiang, and K. Shimizu, Analytical Electron-Microscope Study on the Bainitic Transformation in Beta-Phase Cu-Zn-Au Alloys, *Mater. Trans. JIM*, 1991, **32**(8), p 757–765.
 43. B.C. Muddle, J.F. Nie, and G.R. Hugo, Application of the Theory of Martensite Crystallography to Displacive Phase Transformations in Substitutional Nonferrous Alloys, *Metall. Mater. Trans. A.*, 1994, **25**(9), p 1841–1856.
 44. M.H. Wu, J. Perkins, and C.M. Wayman, Long Range Order, Antiphase Domain Structures, and the Formation Mechanism of α_1 (“Bainite”) Plates in A Cu-Zn-Al alloy, *Acta Metall.*, 1989, **37**(7), p 1821–1837.
 45. K. Takezawa, and S. Sato, Nucleation and Growth of Bainite Crystals in Cu-Zn-Al Alloys, *Metall. Trans. A*, 1990, **21**(6), p 1541–1545.
 46. L.-G. Bujoreanu, On the Influence of Austenitization on the Morphology of α -Phase in Tempered Cu–Zn–Al Shape Memory Alloys, *Mater. Sci. Eng. A*, 2008, **481–482**, p 395–403.
 47. Y. Sutou, N. Koeda, T. Omori, R. Kainuma, and K. Ishida, Effects of Ageing on Bainitic and Thermally Induced Martensitic

- Transformations in Ductile Cu–Al–Mn-Based Shape Memory Alloys, *Acta Mater.*, 2009, **57**(19), p 5748–5758.
48. S. Motomura, T. Hara, T. Omori, R. Kainuma, and M. Nishida, Morphological and Chemical Analysis of Bainite in Cu-17Al-11Mn (at%) Alloys by Using Orthogonal FIB-SEM and Double-EDS STEM, *Microscopy (Oxf)*, 2016, **65**(3), p 243–252.
 49. R. Lagneborg, The Martensite Transformation in 18% Cr-8% Ni Steels, *Acta Metall.*, 1964, **12**(7), p 823–843.
 50. P.L. Mangonon, and G. Thomas, The Martensite Phases in 304 Stainless Steel, *Metall. Trans.*, 1970, **1**(6), p 1577–1586.
 51. G.B. Olson, and M. Cohen, A Mechanism for the Strain-Induced Nucleation of Martensitic Transformations, *J. Less Common Met.*, 1972, **28**(1), p 107–118.
 52. Y. Wada, N. Nakada, and S. Onaka, Internal Stress of Plate Martensite Depending on Aspect Ratio via fcc-hcp Martensitic Transformation in Metastable Austenitic Stainless Steels, *Mater. Trans.*, 2020, **61**(1), p 61–67.
 53. K.I. Shimizu, and Y. Tanaka, The $\gamma \rightarrow \varepsilon \rightarrow \alpha'$ Martensitic Transformations in an Fe–Mn–C Alloy, *Trans. J. Inst. Met.*, 1978, **19**(12), p 685–693.
 54. W.Y. Jang, Q. Gu, J. Van Humbeeck, and L. Delaey, Microscopic Observation of γ -Phase and ε - and α' -Martensite in Fe–Mn–Si-Based Shape Memory Alloys, *Mater. Charact.*, 1995, **34**(2), p 67–72.
 55. S.T. Pisarik, and D.C. Van Aken, Crystallographic Orientation of the $\varepsilon \rightarrow \alpha'$ Martensitic (Athermal) Transformation in a FeMnAlSi Steel, *Metall. Mater. Trans. A.*, 2014, **45**(8), p 3173–3178.
 56. Y. Tsuchiya, T. Bitoh, S. Murayama, S. Chikazawa, and Y. Hamaguchi, Magnetic Properties and Magnetic Phase Diagram of bcc Cr–Fe–Mn Alloys, *J. Phys. Soc. Jpn.*, 1996, **65**(10), p 3289–3293.
 57. B. Li, H.L. Alberts, A.M. Strydom, B.M. Wu, A.R.E. Prinsloo, and Z.J. Chen, Magnetic Properties of Cr–Fe–Mn Alloys, *J. Magn. Magn. Mater.*, 2009, **321**(2), p 61–73.
 58. R.J. Weiss, and K.J. Tauer, Components of the Thermodynamic Functions of Iron, *Phys. Rev.*, 1956, **102**(6), p 1490–1495.
 59. L. Kaufman, E.V. Clougherty, and R.J. Weiss, The Lattice Stability of Metals—III Iron, *Acta Metall.*, 1963, **11**(5), p 323–335.
 60. T. Omori, K. Ando, M. Okano, X. Xu, Y. Tanaka, I. Ohnuma, R. Kainuma, and K. Ishida, Superelastic Effect in Polycrystalline Ferrous Alloys, *Science*, 2011, **333**(6038), p 68–71.
 61. T. Omori, and R. Kainuma, Martensitic Transformation and Superelasticity in Fe–Mn–Al-Based Shape Memory Alloys, *Shape Memory Superelasticity*, 2017, **3**(4), p 322–334.
 62. T. Nishizawa, Progress of CALPHAD, *Mater. Trans., JIM*, 1992, **33**(8), p 713–722.
 63. T. Nishizawa, Effect of Magnetic Transition on Phase Equilibria in Iron Alloys, *JPE*, 1995, **16**(5), p 379–389.
 64. K. Otsuka, T. Ohba, M. Tokonami, and C.M. Wayman, New Description of Long-Period Stacking Order Structures of Martensites in Beta-Phase Alloys, *Scr. Metall. Mater.*, 1993, **29**(10), p 1359–1364.
 65. K. Ishida, K. Shibuya, and T. Nishizawa, γ -Loops in Fe–Mn–V Fe–Mn–Mo and Fe–Mn–Si Systems, *J. Jpn. Inst. Met.*, 1973, **37**(12), p 1305–1313.
 66. X. Xu, T. Omori, M. Nagasako, A. Okubo, R.Y. Umetsu, T. Kanomata, K. Ishida, and R. Kainuma, Cooling-Induced Shape Memory Effect and Inverse Temperature Dependence of Superelastic Stress in Co2Cr(Ga, Si) Ferromagnetic Heusler Alloys, *Appl Phys Lett*, 2013, **103**(16), p 164104.
 67. X. Xu, M. Nagasako, M. Kataoka, R.Y. Umetsu, T. Omori, T. Kanomata, and R. Kainuma, Anomalous Physical Properties Of Heusler-Type Co2Cr(Ga, Si) Alloys and Thermodynamic Study on reentrant Martensitic Transformation, *Phys. Rev. B*, 2015, **91**(10), p 104434.
 68. T. Odaira, S. Xu, X. Xu, T. Omori, and R. Kainuma, Elastocaloric Switching Effect Induced by Reentrant Martensitic Transformation, *Appl. Phys. Rev.*, 2020, **7**(3), p 031406.

Publisher's Note Springer Nature remains neutral with regard to jurisdictional claims in published maps and institutional affiliations.